Citation for published version:
Shields, P, Le Boulbar, E, Priesol, J, Nouf-Allehiani, M, Naresh-Kumar, G, Fox, S, Trager-Cowan, C, Šatka, A & Allsopp, D 2017, 'Design and fabrication of enhanced lateral growth for dislocation reduction in GaN using nanodashes', *Journal of Crystal Growth*, vol. 466, pp. 30-38. https://doi.org/10.1016/j.jcrysgro.2017.02.047

DOI:
10.1016/j.jcrysgro.2017.02.047

Publication date:
2017

Document Version
Publisher's PDF, also known as Version of record

Link to publication

Publisher Rights
CC BY

University of Bath

Alternative formats
If you require this document in an alternative format, please contact:
openaccess@bath.ac.uk

General rights
Copyright and moral rights for the publications made accessible in the public portal are retained by the authors and/or other copyright owners and it is a condition of accessing publications that users recognise and abide by the legal requirements associated with these rights.

Take down policy
If you believe that this document breaches copyright please contact us providing details, and we will remove access to the work immediately and investigate your claim.

Download date: 25. Jun. 2024

Journal of Crystal Growth 466 (2017) 30–38

Contents lists available at ScienceDirect

Journal of Crystal Growth

journal homepage: www.elsevier.com/locate/crys

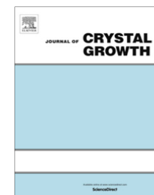

Design and fabrication of enhanced lateral growth for dislocation reduction in GaN using nanodashes

E.D. Le Boulbar [a], J. Priesol [b], M. Nouf-Allehiani [c], G. Naresh-Kumar [c], S. Fox [a], C. Trager-Cowan [c], A. Šatka [b,d], D.W.E. Allsopp [a], P.A. Shields [a,*]

[a] Department of Electronic and Electrical Engineering, University of Bath, BA2 7AY, UK
[b] Institute of Electronics and Photonics, Slovak University of Technology, Ilkovicova 3, 81219 Bratislava, Slovakia
[c] Department of Physics, SUPA, Strathclyde University, Glasgow, G4 0NG, UK
[d] International Laser Centre, Ilkovicova 3, 84104 Bratislava, Slovakia

ARTICLE INFO

Article history:
Received 10 October 2016
Received in revised form 26 January 2017
Accepted 27 February 2017
Available online 1 March 2017
Communicated by T.F. Kuech

Keywords:
A1. Defects
A3. Metalorganic chemical vapour epitaxy
A3. Pendeoepitaxy
A3. Selective epitaxy
B1. Nitrides
B2. Semiconducting III-V materials

ABSTRACT

The semiconductor gallium nitride is the material at the centre of energy-efficient solid-state lighting and is becoming increasingly important in high-power and high-frequency electronics. Reducing the dislocation density of gallium nitride planar layers is important for improving the performance and reliability of devices, such as light-emitting diodes and high-electron-mobility transistors. The patterning of selective growth masks is one technique for forcing a three-dimensional growth mode in order to control the propagation of threading defects to the active device layers. The morphology of the three-dimensional growth front is determined by the relative growth rates of the different facets that are formed, and for GaN is typically limited by the slow-growing {1 −1 0 1} facets. We demonstrate how the introduction of nanodash growth windows can be oriented in an array to preserve fast-growing {1 1 −2 2} facets at the early stage of growth to accelerate coalescence of three-dimensional structures into a continuous GaN layer. Cathodoluminescence and Electron Channelling Contrast Imaging methods, both used to measure the threading dislocation density, reveal that the dislocations are organised and form a distinctive pattern according to the underlying mask. By optimising the arrangement of nanodashes and the nanodash density, the threading dislocation density of GaN on sapphire epilayers can be reduced significantly from 10^9 cm^{-2} to 3.0×10^7 cm^{-2}. Raman spectroscopy, used to monitor the strain in the overgrown GaN epilayers, shows that the position of the GaN E_2^H phonon mode peak was reduced as the dash density increases for a sample grown via pendeo-epitaxy whilst no obvious change was recorded for a sample grown via more conventional epitaxial lateral overgrowth. These results show how growth mask design can be used to circumvent limitations imposed by the growth dynamics. Moreover, they have revealed a greater understanding of the influence of the growth process on the dislocation density which will lead to higher performing electronic and optoelectronic devices as a result of the lower dislocation densities achieved.

© 2017 The Authors. Published by Elsevier B.V. This is an open access article under the CC BY license (http://creativecommons.org/licenses/by/4.0/).

1. Introduction

The electronic and optoelectronic properties of gallium nitride and its alloys are widely exploited for the creation of electronic and optoelectronic devices. The performance of these devices depends to a large extent on the quality of the semiconductor crystal, with the effect that continuing improvements are continuously sought. Efforts are focussed on the improvement of semiconductor growth via techniques such as molecular beam epitaxy (MBE), metal-organic vapour phase epitaxy (MOVPE), hydride phase epitaxy (HVPE) and liquid phase epitaxy (LPE), notably on the control of growth through the intrinsic growth parameters, and through external influences. The latter is exemplified by the use of selective masks on the growth substrate to influence the morphology of the subsequent growth, resulting in epitaxial lateral overgrowth [1].

In the past few years there has been substantial interest in the use of nanorods to create planar GaN epilayers with reduced dislocation density through dislocation bending and annihilation [1–4] and reduced strain [5–8] in order to mitigate the use of thermal- and lattice-mismatched substrates. Such improvements will lead to longer device lifetimes, and superior performance [9]. Another benefit of the nanorod interlayer is a consequence of the reduced

* Corresponding author.
E-mail address: p.shields@bath.ac.uk (P.A. Shields).

http://dx.doi.org/10.1016/j.jcrysgro.2017.02.047
0022-0248/© 2017 The Authors. Published by Elsevier B.V.
This is an open access article under the CC BY license (http://creativecommons.org/licenses/by/4.0/).

foot-print of the overgrown layer on the original substrate. This results in the interlayer being a natural cleavage plane which can be used for the manufacture of thick free-standing substrates [7,8] or the release of device layers onto more appropriate carrier substrates in, for example, a flip-chip vertical LED process.

The concept of coalescence from nanorod tips can be implemented in different ways. There are two essential steps: the formation of a nanorod array, and the coalescence. The creation of the nanorod array can be via a bottom-up growth method, such as MBE, MOVPE or HVPE or via top-down etching of a planar film [10,11]. Most previous reports have aimed to maintain the voids between nanorods to allow three-dimensional strain relaxation at the nanorod interlayer, though Refs. [8,12] are notable in that dislocation reduction has been achieved even with complete infilling. The preservation of voids has generally been achieved through consideration of the growth mechanism preventing lateral growth near their base. For MBE-grown nanorods coalesced by MBE the growth conditions can be changed to promote lateral growth solely at the nanorod tips [5,6,13,14] or by exploiting their high aspect ratio if coalesced by MOVPE [7,15]. Alternatively the nanorod sidewalls can be coated with a selective growth mask to only allow overgrowth from the nanorod tips [8,16,17].

MOVPE overgrowth from the tips of nanorods relies on lateral growth to bridge the gap between neighbouring nanorods to create a planar GaN layer. Growth from a localised seed region, such as at the nanorod tip, evolves through facet competition to result in a morphology that is defined by the slowest growing crystal facets. It is well known that under a wide range of growth parameters MOVPE growth gives rise to {1 −1 0 1} facets that grow much slower than most other facets. Therefore coalescence between neighbouring nanorods relies on the controlled expansion and coalescence of nanopyramids. Previously the use of overgrowth from a one-dimensional array of stripes aligned along ⟨1 −1 0 0⟩ forced lateral growth with faster facets such as {1 1 −2 2}. However, this led to different strain parallel and perpendicular to the stripes and a distinct tilt in the direction of the *c*-axis in the laterally-grown 'wing' regions. A more symmetric two dimensional pattern would avoid this in-plane anisotropy in parameters such as the mechanical strain.

In this paper, we introduce a pattern designed to reduce the influence of the slow-growing {1 −1 0 1} nanopyramid facets to the final overgrown layer. This is achieved by elongating the circular nanorod geometry into an elliptical or rectangular 'nanodash' shape, where the major axis is aligned carefully to the underlying crystal orientation. The use of nanodashes enables controlled lateral growth via the faster growing {1 1 −2 2} lateral facets. We describe the growth experiments used to evaluate the process and show the impact of different patterns, which affect the areal dash density, on the density and distribution of dislocations. The latter are characterised by cathodoluminescence (CL) and Electron Channelling Contrast Imaging (ECCI). The impact of the patterning on the strain of the GaN overgrown layer is investigated by Raman spectroscopy.

2. Epitaxial growth

2.1. Growth evolution of individual nanodashes

Selective area growth is a technique used to constrain the location of epitaxial growth by defining regions where further material cannot nucleate. Typically in the growth of GaN by MOVPE, dielectric layers of SiO_2 or SiN_x are patterned on top of a GaN layer to reveal windows of GaN where growth can occur surrounded by dielectric that does not support nucleation.

Initial growth tests were performed to demonstrate the effect of elongating a circular growth window on the morphology of the regrowth. Electron beam lithography combined with dry etching was used to define on a GaN template windows in a thin dielectric layer with dimensions 500 × 2500 nm as shown in the secondary electron (SE) images in Fig. 1a and e. The pattern windows on each sample were oriented at differing angles from the ⟨1 −1 0 0⟩ direction; ranging from 0 to 40° in steps of 5°. MOVPE growth in a horizontal flow Aixtron 200/4HT RF-S reactor using a nominal temperature of 965 °C, reactor pressure 100 mbar, Ga flow of 20 sccm and a V/III ratio of 2700 was performed for growth durations from 2 to 80 min. SE images corresponding to alignment along ⟨1 −1 0 0⟩ and ⟨1 1 −2 0⟩ are shown in Fig. 1 and show the evolution of growth for these two orientations with different growth times.

Initial growth is expected to comprise random nucleation within the GaN window with fast c-plane growth subsequently creating a rough, facetted morphology as can be seen in Fig. 1b and f. Coalescence of these nucleation sites within the region defined by the growth mask leads to the gradual extinction of all the faster growing facets leaving large areas of slower growing {1 −1 0 1} and {1 1 −2 2} facets at the edge of the growth mask. With further growth, material is preferentially added to the {1 1 −2 2} planes due to the higher growth rate (Fig. 1d), in accordance with the dynamic Wulff theory in which the final feature shape for convex growth is determined by the slowest crystal planes[18,19]. Thus, the {1 1 −2 2} planes are eventually eliminated so that the shape of the final structure is determined by the alignment of the window opening relative to the crystallographic planes as demonstrated by a comparison of Fig. 1d and h.

For a given growth time, the feature area is strongly dependent on the angle of alignment due to the enhanced lateral growth for features aligned along ⟨1 −1 0 0⟩. Fig. 2a shows a comparison between the average area covered by the regrowth for features aligned along ⟨1 −1 0 0⟩ and ⟨1 1 −2 0⟩. Initially (the first 20 min of growth) the rate of increase of area is 3.5 times higher for ⟨1 −1 0 0⟩ than ⟨1 1 −2 0⟩ aligned features. Subsequently the rate of area increase for ⟨1 −1 0 0⟩ aligned features asymptotically reduces to match that of ⟨1 1 −2 0⟩ aligned features. At this transition the faster growing {1 1 −2 2} facets have been eliminated to leave only the slow-growing {1 1 0 1} facets as shown in Fig. 1d and h. The dependence on alignment angle is shown in Fig. 2b for 20 min growth.

2.2. Design of nanodash arrays

In order to create a coalesced planar layer with a reduced dislocation density, nanodash arrays were designed and fabricated. In designing a pattern to tile the nanodashes onto a 2D plane there were two aims: (1) to retain the highest degree of symmetry possible in order to avoid the non-circularly-symmetric bow that occurs in stripe epitaxial lateral overgrowth (ELOG), and (2) to maintain a high lateral growth velocity by maintaining for as long as possible {1 1 −2 2} or other higher index planes in addition to the slow growing {1 −1 0 1} planes. Growth on such localised regions as the nanodashes is inherently convex and will eventually be dominated by the slowest growing planes. As shown in Fig. 2, one can extend the time for which faster growth planes are present by aligning the nanodashes along ⟨1 −1 0 0⟩, hence accelerate the lateral growth and thus reduce the growth window density. This potentially allows for minimal contact points with the substrate for strain relaxation, possible substrate removal, and greater dislocation filtering.

In the simplest implementation of the idea, the growth proceeds in the order: convex – concave – planarization, as explained below. The hexagonal-symmetry-breaking nanodashes aligned along ⟨1 −1 0 0⟩ are used to promote lateral growth during the

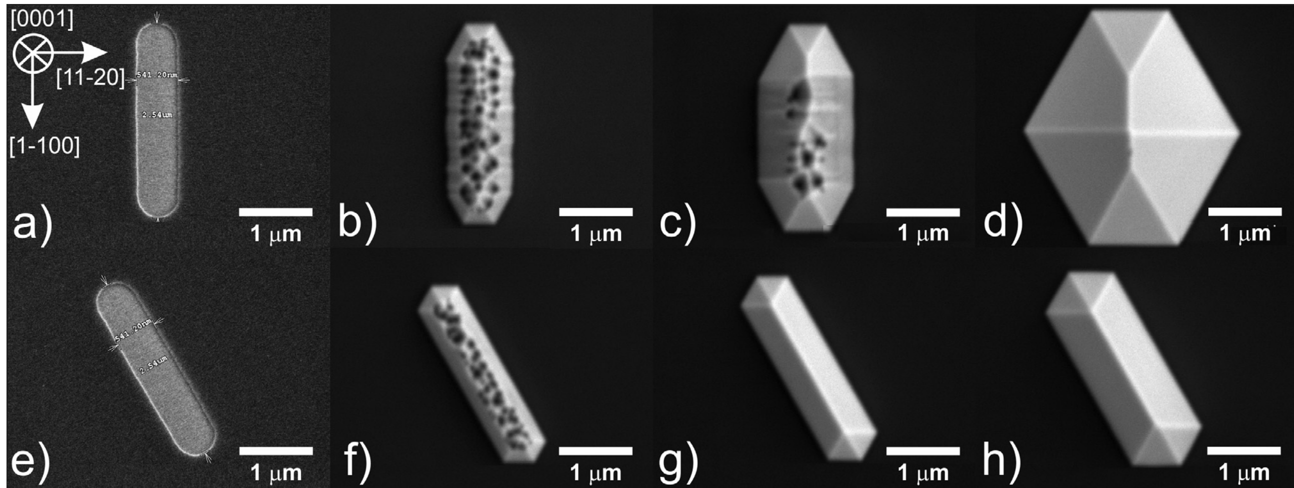

Fig. 1. Evolution of the selective area growth from a nanodash-shaped window in a selective growth mask. (a) and (e) show the growth window prior to MOVPE growth with (b) and (f) after 2 min, (c) and (g) after 5 min, and (d) and (h) after 20 min regrowth. The growths in (b) to (d) are aligned along ⟨1 −1 0 0⟩ whilst those in (f) to (h) are aligned along ⟨1 1 −2 0⟩.

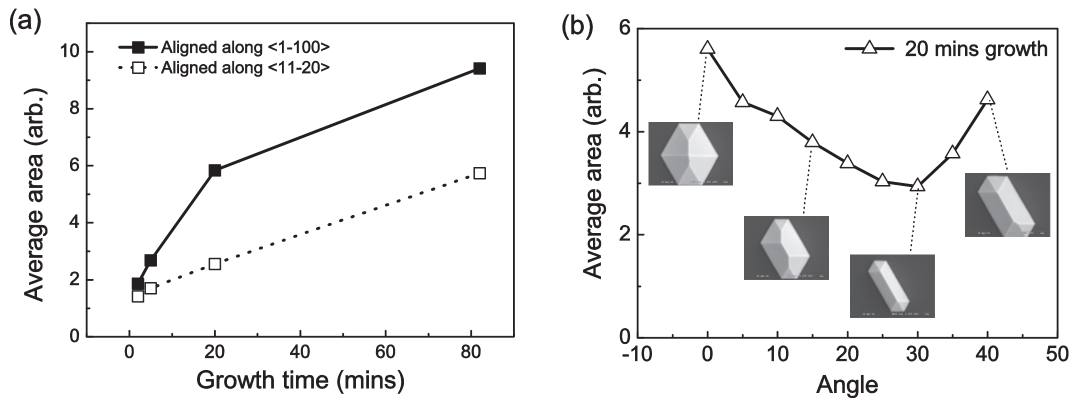

Fig. 2. (a) Increase in the average area (projection onto the c-plane) versus growth time for the nanodash windows in Fig. 1 aligned along the ⟨1 −1 0 0⟩ and ⟨1 1 −2 0⟩ directions. (b) Average area for 20 min growth for differing deviations of alignment from the ⟨1 −1 0 0⟩ direction.

convex growth phase. If neighbouring nanodashes meet before the non-{1 −1 0 1} crystal planes have been eliminated by their fast growth, the growth switches from convex to concave growth. This can be achieved by a careful arrangement of the pattern. Once the growth has switched to concave growth, the growth rate increases and the symmetry can remain hexagonal to match the symmetry of the crystal until the onset of planarization. Therefore, since there are three different possible orientations of the nanodash along the family of ⟨1 −1 0 0⟩ directions, they should be combined into a basis and then tiled using a hexagonal Bravais lattice. In this work the basis, tiled hexagonally, consists of three nanodashes orientated along the ⟨1 −1 0 0⟩ directions. The nanodashes are then positioned relative to each other so that at the point where the {1 1 −2 2} planes are eliminated, the expanding wing of one nanostructure touches the corner of a neighbouring nanostructure.

Fig. 3 shows a set of patterned growth templates with nanodash-array selective-growth masks that follow the design rules described above. Within different regions of the templates the nanodashes have differing aspect ratios which lead to varying filling factors. The samples were obtained via nanoimprint lithography using a fabrication method that can be found elsewhere [20–22]. Two different types of template were prepared. In the first, shown in Fig. 3a–c, the region between the nanodashes was etched to a depth of 700 nm in order to leave nanodash pillars. The etched region was subsequently passivated with a combination of SiN_x and hydrogen silsesquioxane (HSQ) in order to ensure growth only from the nanodash pillar top surface. This led to nanopendeo regrowth. The second, shown in Fig. 3d–f, consisted of arrays of nanodash-shaped openings in a thin planar SiN_x layer to allow for more conventional epitaxial lateral overgrowth (ELOG). Each region had different dimensions (length, width, filling factor, nanodash density) which are summarised in Table 1.

2.3. GaN growth from nanodash array patterns

Fig. 4 shows the evolution of the growth morphology with time for a nanodash size of 1.3 × 11 μm (ELOG template/region E). The initial MOVPE growth of GaN was carried out with the following parameters: growth temperature of 925 °C, growth pressure of 100 mbar, trimethyl gallium (TMGa) flow of 5 sccm, NH_3 flow of 1200 sccm (Fig. 4b–f). The TMGa and NH_3 flows were then increased in order to increase the growth rate (TMGa flow of 20 sccm, NH_3 flow of 1600 sccm) (Fig. 4g). Finally the temperature was increased from 925 °C to 1050 °C in order to planarize the surface (Fig. 4i).

After the first 20 min of growth, a highly regular pattern of elongated pyramid dashes is grown (Fig. 4c). Each dash is made up of six slow-growing {1 −1 0 1} facets and two fast-growing {1 1 −2 2} facets, the latter laterally enlarging the nanostructures to create more diamond-like shapes. At the point of coalescence of

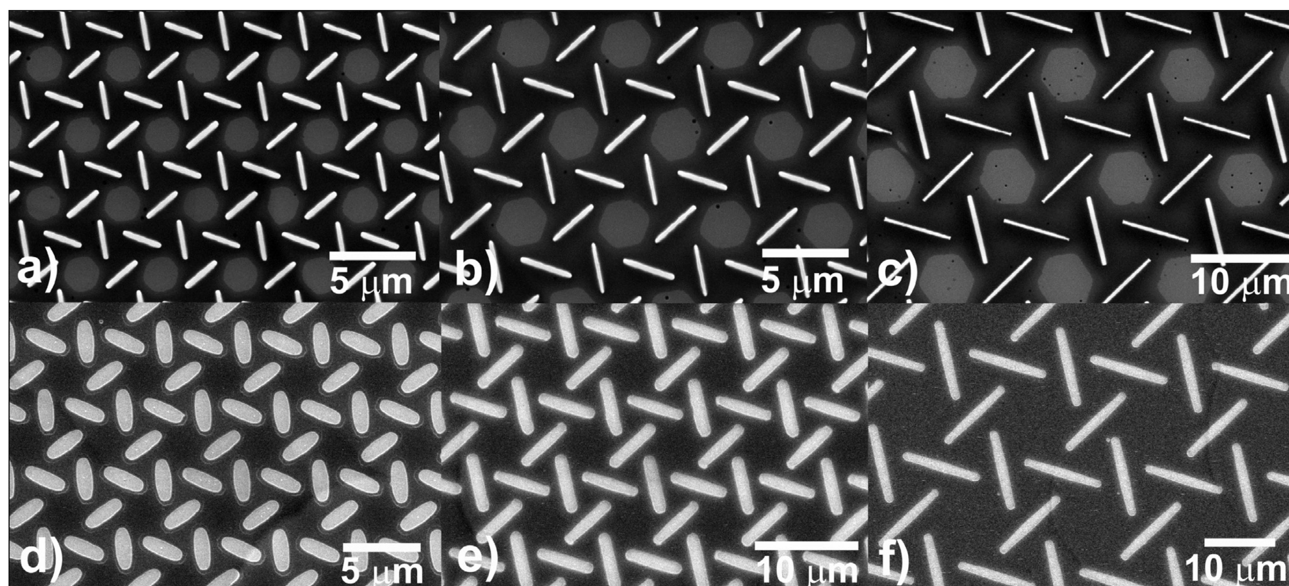

Fig. 3. Scanning electron microscopy plan-view secondary electron images of the templates prepared for nanopendeo regrowth (upper) and ELOG (lower): (a) and (d) region A, (b) region B, (c) region D, (e) region C, (f) region E.

Table 1
Summary of the dash dimensions obtained for both nanopendeo and ELOG templates.

Nanopendeo				ELOG				Dash density (cm^{-2})
Region	Mean length (μm)	Mean width (nm)	Filling factor (%)	Region	Mean length (μm)	Mean width (nm)	Filling factor (%)	
A	2	250	10.7	A	2.4	750	36	1.5×10^7
B	2.8	175	8	B	3.2	900	34	9.2×10^6
C	5	275	6.1	C	5.6	1200	26	4.2×10^6
D	6.5	450	5.7	D	7.6	1500	24	2.6×10^6
E	10	300	4.1	E	11	1300	16	1.2×10^6

neighbouring dashes, occurring after 200 min growth, {11−22} facets from one structure touch the {1−101} facets of one adjacent (Fig. 4e). At this point the growth front changes from being convex to concave with the formation of new facets with a higher growth rate (Fig. 4e). A hexagonal pattern emerges so that after 440 min growth the structure consists of a highly regular tessellation of {1−101} and (0001) c-plane facets (Fig. 4f). Surprisingly no {11−22} fast growth facets are observed at this stage despite the concave growth front. With further growth, the selective growth mask is completely covered to create an array of large inverted pyramids, each bounded by two coexisting families of planes (denoted S and R in Fig. 4h where R refers to the {1−101} slow growing facets), as has been previously demonstrated during the growth of GaN in an inner circle [23]. Therefore, the concave mode growth has eventually encouraged the emergence of faster growing planes as expected. Planarization at the higher growth temperature was initiated once the growth mask was completely covered to result in c-plane GaN with slight undulations in the surface (Fig. 4i).

3. Characterisation

3.1. Cathodoluminescence and electron channelling contrast imaging

Cathodoluminescence (CL) imaging was used to assess the impact of the nanodash pattern on the arrangement and density of dislocations. CL imaging is a non-destructive method based on the non-radiative recombination at dislocations. The TDD estimates obtained via CL were also compared with those obtained using Electron Channelling Contrast Imaging (ECCI) [24]. ECCI has a higher resolution than CL and can provide further details on the type of dislocations present [25].

A field-emission gun scanning electron microscope (SEM) LEO1550 combined with a Gatan MonoCL4 CL detection system was employed. An electron acceleration voltage of 5 kV and a beam current below 1 nA were used to avoid the radiation damage and preserve the lateral resolution during the panchromatic SEM CL imaging. The samples were at room temperature.

Fig. 5a displays a representative CL image of region E of the ELOG pattern that has been used to assess the dislocation density after the planarization step. Two main features can be identified: (i) the clustering of dislocations in a periodic pattern with the circular clusters (red circles) surrounded by an area of lower dislocation density, and (ii) the arrangement of other groups of dislocations along distinct lines, angled at 60 degree intervals (green lines). In Fig. 5a, circular clusters are hexagonally arranged with a spacing of 11.5 μm. Fig. 5b and c show a CL image from a planarized sample superimposed onto SEM images of the same sample at earlier stages of growth using the circular dislocation clusters for the registration of the images. It can be clearly seen that the dark spot clusters correlate with the pattern of large inverted pyramids shown in Fig. 4g whilst the dislocation lines are aligned along the ⟨11−20⟩ directions. An overlay of the CL on an image of the selective growth mask (Fig. 5b) demonstrates that only a very small proportion of the total number of defects propagate through the growth window, verifying that efficient cancellation or bending of dislocations occurs during the initial stages of growth. This figure also shows that some regions covering

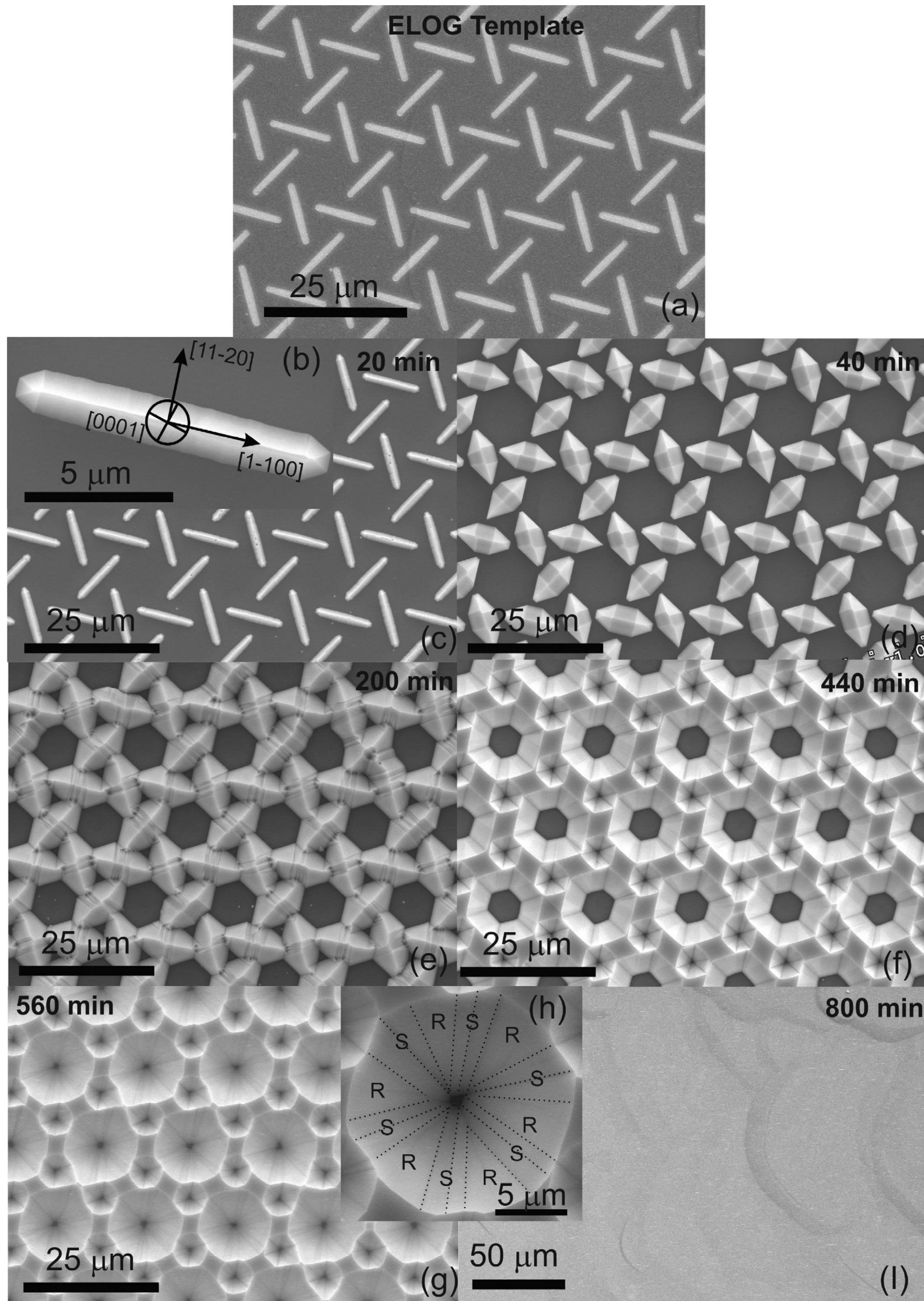

Fig. 4. Secondary electron images taken at different stages of growth from region E of the ELOG sample. (a) Dash-shaped selective growth windows. (b and c) Initial growth within window bounded by {1 −1 0 1} & {1 1 −2 2} facets. (d) Further dash growth predominantly via the {1 1 −2 2} faster-growth facet. (e) First coalescence step – merging of individual dashes. (f) Appearance of hexagons composed of {1 −1 0 1} facets interspersed with (0 0 0 1) c-plane facets. (g and h) Coexistence of higher indexes facets with slow-growing facets. (i) Planarization.

the first coalescence of the dashes are defect free, implying that either the dislocations generated at the coalescence boundaries are mobile as the growth proceeds, or none are created. Overlay of the CL on the large inverted pyramids (Fig. 5c) shows a perfect alignment between the dislocations aligned along ⟨1 1 −2 0⟩ and the edge of {1 −1 0 0} facets forming the inverted pyramid. The organisation of dislocations in clusters and lines, with an identified pattern, suggests dislocations are propagated along preferential directions and merge at a single and unique point. An alternative explanation is that lines of defects along the ⟨1 1 −2 0⟩ directions could have been created by the coalescence between opposite {1 −1 0 1} planes.

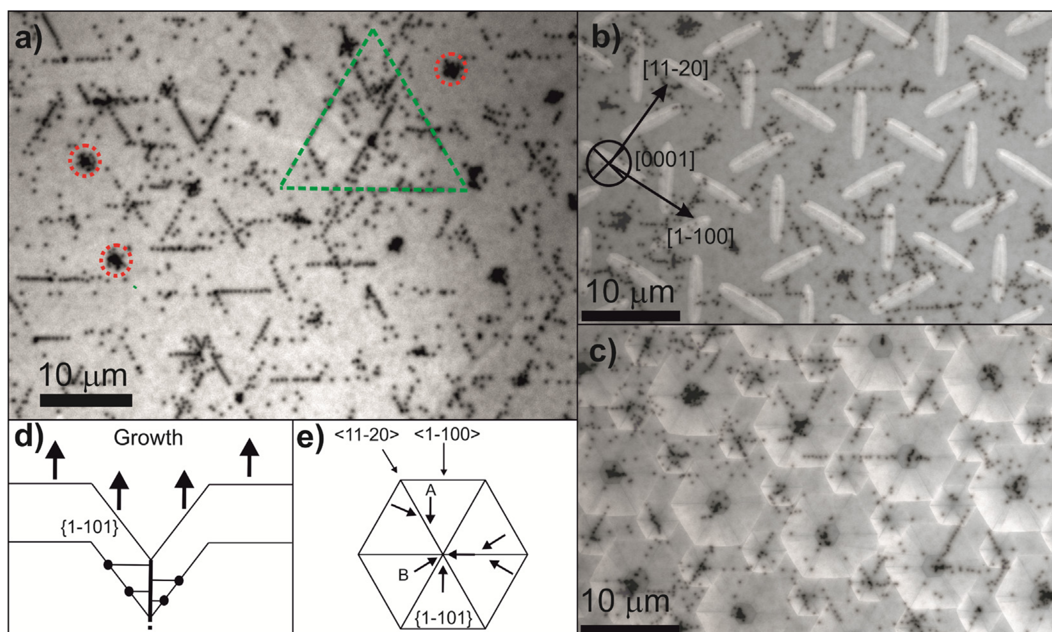

Fig. 5. (a) Panchromatic CL image of the region E obtained via ELOG. (b) CL image superimposed with scanning electron microscopy secondary electron images of the initial selective growth mask, and (c) the inverted pyramids formed mid-growth. Dislocations preferentially follow the ⟨11−20⟩ directions or are concentrated towards the centre of the inverted pyramid. (d) Diagram of the dislocation propagation from the surface of the facets to the centre of the inverted pyramid (e) plan-view of the dislocation propagation route within the hexagonal pit.

A model of dislocation reduction involving inverted pyramids bounded by {11−22} facets has been proposed by Motoki et al. [26]. This model can be extended to inverted pyramids bounded by {1−101} facets or even by a combination of {1−101} and {11−22} facets as suggested by Fig. 4h. When a hexagonal pyramidal pit formed by {1−101} facets grows, dislocations existing on the surface of the facets move parallel to the (0001) plane mainly in the ⟨1−100⟩ directions (as depicted in Fig. 5d) and concentrate towards the centre of the pit (e.g. for a dislocation at position B in Fig. 5e) and along the intersections with the other {1−101} facets (e.g. for a dislocation at position A in Fig. 5e). Other dislocations located close to A would move in a similar way to create a dislocation line array parallel to ⟨11−20⟩ marking the {1−101} facet intersections. These are visible as line arrays in the CL from the planarized sample due to their redirection along [0001]. Alternatively these dislocations could be redirected along ⟨11−20⟩ and move towards the centre of the inverted pyramid and then are subsequently re-directed along [0001] together with others, such as in position B, that have reached the centre more directly.

A striking feature of the arrangement of dislocations shown in Fig. 5a is how well-defined are the line arrays of dislocations along ⟨11−20⟩. From this, one can deduce that the dislocations are bent along [0001] early in the growth prior to the emergence of the higher index facets as shown in Fig. 4g and h. Such facets would remove the significance of the {1−101} facet intersections along ⟨11−20⟩ and introduce other arbitrary directions for the facet intersections that would change as the growth proceeds.

3.2. Assessment of dislocation density

Dislocations in CL images can be identified by the dark spots that are created due to the capture of excited carriers by the non-radiative recombination route. The size of the dark spot is caused by the minority carrier diffusion length [27] whilst their contrast is determined by the defect carrier capture cross-section. Therefore any measurement of the dislocation density via CL images is highly dependent on the method of estimating the number of dark spots in the agglomerated regions where the close proximity of the defects causes the dark spots to overlap. In this paper we have determined the dark spot area corresponding to individual defects for each image using isolated defects in the low defect density regions. Then to estimate the lower limit for the defect density within each dark spot cluster, the area of the cluster was divided by the average area of one individual dark spot. In order to compare the dislocation density for the different pattern dimensions, panchromatic CL was recorded for every region. Dislocation densities were obtained by counting the dark spots and dividing by the entire surface recorded (i.e. $35 \times 25\ \mu m^2$). An average of seven CL images taken from different places was used to accurately assess the dislocation density for each region. A representative picture of the CL for each region with its TD density is displayed in Fig. 6.

ECCI was used to confirm the accuracy and estimate the error resulting from using CL as a technique for measuring TDD. Whilst CL does not require precise crystallographic alignment, ECCI provides a better resolution than CL so that dislocations can be clearly distinguished within clusters. An example is shown in Fig. 7, where the ECCI images were acquired with an electron beam spot of approximately 4 nm, a beam current of approximately 2.5 nA, a beam divergence of approximately 4 mrad, and an electron beam energy of 30 keV. Furthermore, ECCI allows the determination of dislocation type. Specifically, in region D of the ELOG sample (Fig. 7c), it was determined that edge and screw/mixed dislocations were present in relatively equal proportions, with 50% identified as edge dislocations, 46% as screw/mixed dislocations and 4% unidentified. This identification correlates with an equivalent proportion of edge and screw dislocations in coalesced GaN films reported earlier [1]. ECCI images were recorded from regions D and E of the ELOG samples to give dislocation densities of $4.2 \times 10^7\ cm^{-2}$ and $2.9 \times 10^7\ cm^{-2}$, respectively from image sizes of $35 \times 25\ \mu m^2$.

The values for the TDD from ECCI and CL agree within the error estimated for the CL results as determined from the variation from different imaged areas (see Fig. 8). A more accurate quantitative

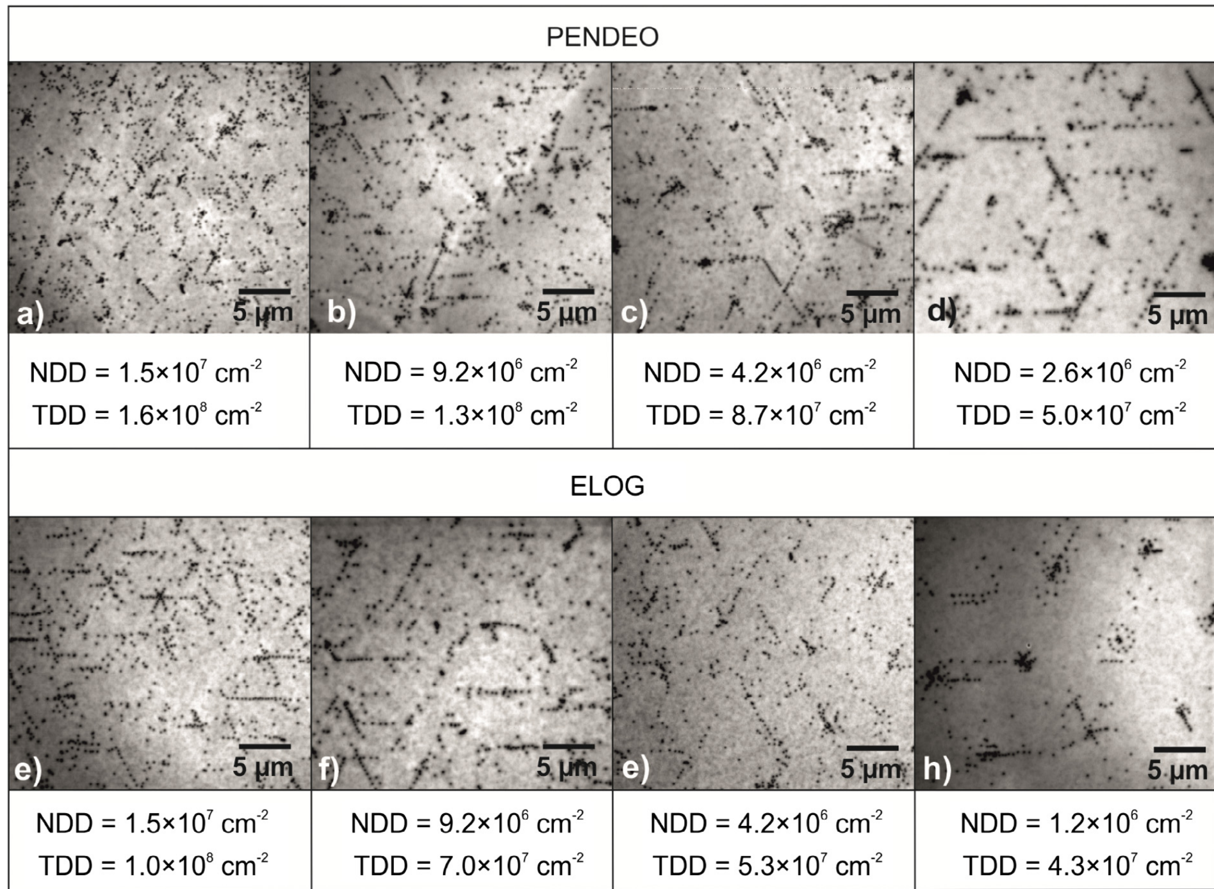

Fig. 6. Panchromatic CL images, related nanodash densities (NDD) and threading dislocation densities (TDD) obtained for pendeo (a) region A, (b) region B, (c) region C, (d) region D and ELOG samples (e) region A, (f) region B, (g) region C, (h) region E.

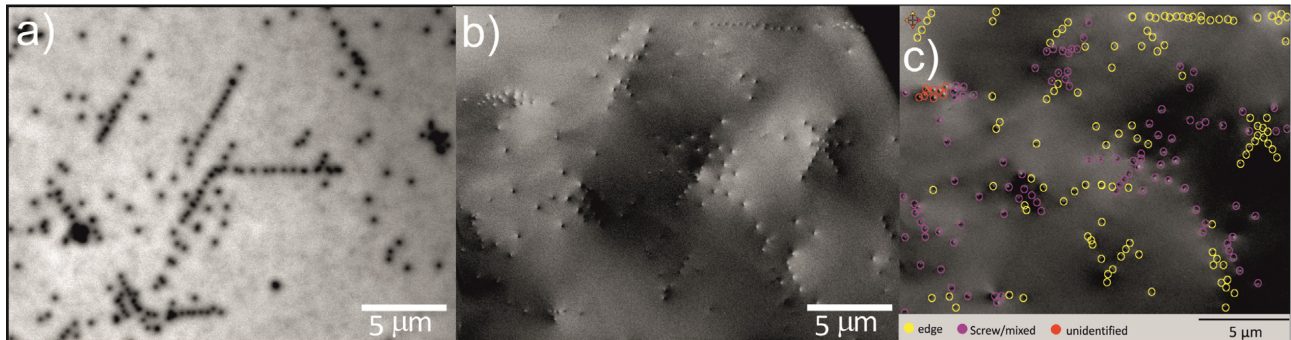

Fig. 7. Cathodoluminescence (a) and ECCI (b) images for region D of the ELOG sample. Note the region of the sample imaged is not the same. The ECCI image in (b) has been annotated in (c) to show the type of dislocation: edge (yellow), screw/mixed (purple), unidentified (red). (For interpretation of the references to colour in this figure legend, the reader is referred to the web version of this article.)

comparison would require the same region to be imaged by the two techniques since the measurements are dominated by sample inhomogeneity.

3.3. Optimisation of pattern for dislocation reduction

The degree of reduction in TDD was found to be strongly dependent on the nanodash density, as shown in Fig. 8. A large increase of the efficacy of the design is observed as the dash density is reduced for both the ELOG and the pendeo technique. For ELOG we note that as the dash density decreases from $1.5 \times 10^7\,\text{cm}^{-2}$ to $1.2 \times 10^6\,\text{cm}^{-2}$, the TDD decreases almost linearly from $1.0 \times 10^8\,\text{cm}^{-2}$ to $4.3 \times 10^7\,\text{cm}^{-2}$. In the case of the pendeo technique, a similar trend has been found, though higher TDD was calculated overall; $5 \times 10^7\,\text{cm}^{-2}$ from region D via CL (Fig. 6d, dash density: $2.6 \times 10^6\,\text{cm}^{-2}$). A weaker linear trend was also found between the TDD and the filling factor, especially for the ELOG sample series. However, if dislocation filtering was the dominant process as a result of the ratio of the areas of the nanodashes to the overall surface, one would have expected the sample series grown with the nanopendeo technique to have lower TDD, in the range $1\text{–}2 \times 10^7\,\text{cm}^{-2}$. Whilst drawing comparisons between the two techniques is not trivial, as discussed below, the measured values are almost an order of magnitude higher, thus suggesting a lesser role of the filling factor than the dash density.

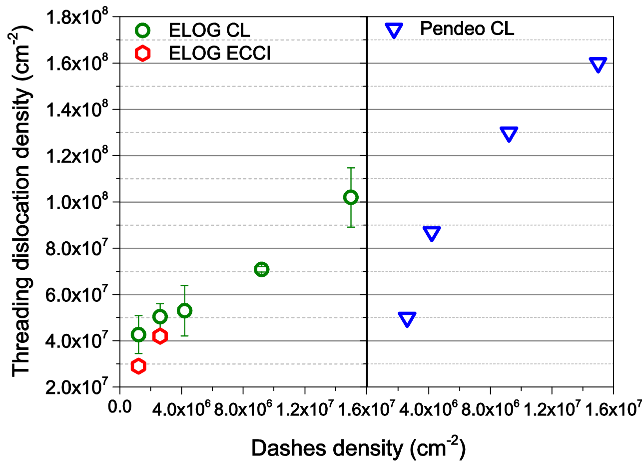

Fig. 8. Threading dislocation density as a function of dash density for ELOG and pendeo samples.

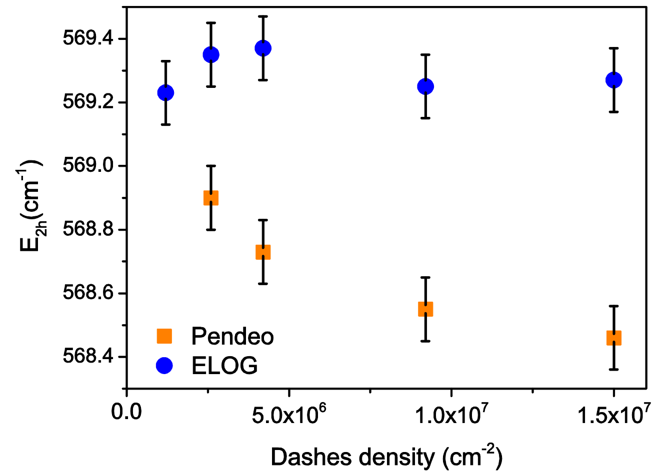

Fig. 9. E_2^H phonon mode peak position measured by Raman spectroscopy on ELOG and pendeo samples as a function of dash density.

The linear dependency of TDD as a function of dash density suggests that the TDD is related to the dislocation regeneration upon GaN coalescence events: the design reduces the density of coalescence events as the number of dashes decrease, which leads to a reduction of TDD. These TDD are much lower than those obtained using conventional growth techniques, which give TDDs in the mid-10^8 cm^{-2} for GaN films grown on c-plane sapphire using low-temperature nucleation layers but without separate ex-situ patterning [28]. Nevertheless, our results show similar trends with those obtained by epitaxially growing around silica microspheres, for which a decrease of TDD from 7.0×10^8 cm^{-2} down to 3.9×10^7 cm^{-2} whilst increasing the sphere diameter form 0.5 to 3 μm was observed [29].

Consistently the dislocation density for each dash density is lower when using the ELOG rather than the pendeo technique. This is despite the growth windows being smaller for the latter, which should, in principle, lead to greater dislocation filtering. This result is likely to be caused by the –*c* plane growth that is free to occur in the pendeo technique but that is blocked in ELOG. From a geometric viewpoint this –*c* plane growth will be first to coalesce. Given that such material has previously been shown to contain a large number of stacking faults [4] and that the final dislocation density is related to dislocation regeneration upon coalescence, this provides a plausible explanation for the difference, although influence of the different fabrication processes prior to regrowth cannot be discounted.

3.4. Assessment of strain in the overgrown GaN layer

An accurate measurement of the position of the GaN E_2^H phonon peak can reveal the strain state in a GaN layer. Raman spectra were taken with a 532 nm laser on every coalesced region for both ELOG and nanopendeo overgrown GaN layers. A strain-free E_2^H value of 567.0 cm^{-1} has been reported in the literature for GaN nanorods whilst the value for a GaN layer grown on sapphire, which is in a compressive state, has a higher value which depends on the strain (from 568.5 to 570.5 cm^{-2}) [30,31]. The E_2^H value for a GaN free-standing wafer is measured as 568.0 cm^{-1}. Kozawa et al. showed the strain in GaN grown on sapphire was reduced as the thickness is increased [32].

An overgrown thickness of 20 μm and 8 μm has been measured from cross-sections imaged via scanning electron microscopy for ELOG and pendeo samples, respectively. This difference in thicknesses suggests that the compressive strain on the overgrown GaN layer should be lower on the ELOG sample than on the pendeo sample. Fig. 9 shows the value of the E_2^H phonon energy measured for each region for both techniques as a function of dash density. For the ELOG growth, the E_2^H peak position for the different regions has been measured to vary by less than 0.1 cm^{-1}, from 569.3 to 569.2 cm^{-1}. In contrast, for the 8-μm-thick GaN layer grown via pendeo on etched GaN nanodashes, a reduction in wavenumber is observed for the E_2^H peak (from 568.9 cm^{-1} to 568.4 cm^{-1}) as the dash density increases, corresponding to a decrease in the compressive strain. This difference of the E_2^H phonon mode wavenumber obtained using these two techniques demonstrates that using etched pendeo nanodashes is appropriate to reduce the built-up strain in GaN layer on sapphire. The lower strain in GaN layers coalesced from the higher density of nanodashes correlates with the higher dislocation density in these regions; the dislocations help the release of compressive strain. A similar behaviour was reported for a GaN layer overgrown on GaN etched nano-islands, as a small reduction in wavenumber was obtained when the nano-island density increased [33].

3.5. Conclusion

We have demonstrated how the use of dash-shaped selective growth windows oriented along $\langle 1\,{-1}\,0\,0\rangle$ directions tiled at a 60° angle could be used as an alternative to circle or stripe openings to obtain very low threading dislocation densities down to ~3.0×10^7 cm^{-2} in planar GaN layers. The dash density was found to have an important impact on the dislocation density, with a lower dash density resulting in lower dislocation density, due to a reduced number of coalescence points. The use of a pendeo epitaxial overgrowth technique revealed that a higher dash density results in better strain accommodation. Cathodoluminescence revealed patterns in the distribution of the dislocations being formed in coalesced GaN layers. Such dislocations are aligned and clustered leaving large areas of dislocation-free material. The predictable locations of the dislocation clusters with respect to the growth windows potentially allows for the alignment of devices in the ultra-low dislocation density regions if the device size is small like GaN-based avalanche photodiodes, small-area detectors or transistors.

Acknowledgements

The work was carried out with partial support from the European Commission (FP7 contract No. 228999: "SMASH"), the

EPSRC, UK (EP/J015792/1, EP/M015181/1) and the Slovak Grant Agency (VEGA 1/0921/13). All data created during this research are openly available from the University of Bath data archive at http://doi.org/10.15125/BATH-00257.

References

[1] P. Gibart, Metal organic vapour phase epitaxy of GaN and lateral overgrowth, Reports Prog. Phys. 67 (2004) 667–715, http://dx.doi.org/10.1088/0034-4885/67/5/R02.
[2] S.D. Hersee, X.Y. Sun, X. Wang, M.N. Fairchild, J. Liang, J. Xu, Nanoheteroepitaxial growth of GaN on Si nanopillar arrays, J. Appl. Phys. 97 (2005) 124308, http://dx.doi.org/10.1063/1.1937468.
[3] T. Tang, C. Lin, Y. Chen, W. Shiao, W. Chang, C. Liao, et al., Nitride nanocolumns for the development of light-emitting diode, IEEE Trans. Electron Devices 57 (2010) 71–78.
[4] C.-N. Huang, P.A. Shields, D.W.E. Allsopp, A. Trampert, Coalescence-induced planar defects in GaN layers grown on ordered arrays of nanorods by metal-organic vapour phase epitaxy, Philos. Mag. 93 (2013) 3154–3166, http://dx.doi.org/10.1080/14786435.2013.805272.
[5] K. Kusakabe, Akihiko Ikuchi, K. Kishino, Characterization of Overgrown GaN Layers on Nano-Columns Grown by RF-Molecular Beam Epitaxy, Overgrown GaN nano, 40 (2001) 194–196.
[6] K. Kusakabe, A. Kikuchi, K. Kishino, Overgrowth of GaN layer on GaN nano-columns by RF-molecular beam epitaxy, J. Cryst. Growth 237–239 (2002) 988–992, http://dx.doi.org/10.1016/S0022-0248(01)02113-3.
[7] Z. Bougrioua, P. Gibart, E. Calleja, U. Jahn, A. Trampert, J. Ristic, et al., Growth of freestanding GaN using pillar-epitaxial lateral overgrowth from GaN nanocolumns, J. Cryst. Growth 309 (2007) 113–120, http://dx.doi.org/10.1016/j.jcrysgro.2007.09.030.
[8] C.L. Chao, C.H. Chiu, Y.J. Lee, H.C. Kuo, P.-C. Liu, J.D. Tsay, et al., Freestanding high quality GaN substrate by associated GaN nanorods self-separated hydride vapor-phase epitaxy, Appl. Phys. Lett. 95 (2009) 051905, http://dx.doi.org/10.1063/1.3195684.
[9] M. Takeya, T. Mizuno, T. Sasaki, S. Ikeda, T. Fujimoto, Y. Ohfuji, et al., Degradation in AlGaInN lasers, Phys. Status Solidi. 2295 (2003) 2292–2295, http://dx.doi.org/10.1002/pssc.200303324.
[10] S. Li, A. Waag, GaN based nanorods for solid state lighting, J. Appl. Phys. 111 (2012) 071101, http://dx.doi.org/10.1063/1.3694674.
[11] P.A. Shields, M. Hugues, J. Zúñiga-Pérez, M. Cooke, M. Dineen, W. Wang, et al., Fabrication and properties of etched GaN nanorods, Phys. Status Solidi. 9 (2012) 631–634, http://dx.doi.org/10.1002/pssc.201100394.
[12] T.-Y. Tang, W.-Y. Shiao, C.-H. Lin, K.-C. Shen, J.-J. Huang, S.-Y. Ting, et al., Coalescence overgrowth of GaN nanocolumns on sapphire with patterned metal organic vapor phase epitaxy, J. Appl. Phys. 105 (2009) 023501, http://dx.doi.org/10.1063/1.3065527.
[13] T.H. Yang, J.T. Ku, J.-R. Chang, S.-G. Shen, Y.-C. Chen, Y.Y. Wong, et al., Growth of free-standing GaN layer on Si(111) substrate, J. Cryst. Growth 311 (2009) 1997–2001, http://dx.doi.org/10.1016/j.jcrysgro.2008.10.099.
[14] D. Cherns, L. Meshi, I. Griffiths, S. Khongphetsak, S.V. Novikov, N. Farley, et al., Defect reduction in GaN/(0001)sapphire films grown by molecular beam epitaxy using nanocolumn intermediate layers, Appl. Phys. Lett. 92 (2008) 121902, http://dx.doi.org/10.1063/1.2899944.
[15] T.-Y. Tang, K.L. Averett, J.D. Albrecht, W.-Y. Shiao, Y.-S. Chen, C.C. Yang, et al., Coalescence overgrowth of GaN nano-columns with metalorganic chemical vapor deposition, Nanotechnology 18 (2007) 445601, http://dx.doi.org/10.1088/0957-4484/18/44/445601.
[16] P. Shields, C. Liu, A. Šatka, A. Trampert, J. Zúñiga-Pérez, B. Alloing, et al., Nanopendeo coalescence overgrowth of GaN on etched nanorod array, Phys. Status Solidi. 8 (2011) 2334–2336, http://dx.doi.org/10.1002/pssc.201000996.
[17] C. Liu, P.A. Shields, Q. Chen, D.W.E. Allsopp, W.N. Wang, C.R. Bowen, et al., Variations in mechanisms of selective area growth of GaN on nano-patterned substrates by MOVPE, Phys. Status Solidi 7 (2010) 32–35, http://dx.doi.org/10.1002/pssc.200982618.
[18] Q. Sun, C.D. Yerino, B. Leung, J. Han, M.E. Coltrin, Understanding and controlling heteroepitaxy with the kinetic Wulff plot: a case study with GaN, J. Appl. Phys. 110 (2011) 053517, http://dx.doi.org/10.1063/1.3632073.
[19] B. Leung, Q. Sun, C.D. Yerino, J. Han, M.E. Coltrin, Using the kinetic Wulff plot to design and control nonpolar and semipolar GaN heteroepitaxy, Semicond. Sci. Technol. 27 (2012) 024005, http://dx.doi.org/10.1088/0268-1242/27/2/024005.
[20] P.A. Shields, D.W.E. Allsopp, Nanoimprint lithography resist profile inversion for lift-off applications, Microelectron. Eng. 88 (2011) 3011–3014, http://dx.doi.org/10.1016/j.mee.2011.04.063.
[21] E.D. Le Boulbar, I. Ĝırgel, C.J. Lewins, P.R. Edwards, R.W. Martin, A. Šatka, et al., Facet recovery and light emission from GaN/InGaN/GaN core-shell structures grown by metal organic vapour phase epitaxy on etched GaN nanorod arrays, J. Appl. Phys. 114 (2013) 094302, http://dx.doi.org/10.1063/1.4819440.
[22] G. Hubbard, S.J. Abbott, Q. Chen, D.W.E. Allsopp, W.N. Wang, C.R. Bowen, et al., Wafer-scale transfer of nanoimprinted patterns into silicon substrates, Phys. E. 41 (2009) 1118–1121, http://dx.doi.org/10.1016/j.physe.2008.08.014.
[23] W. Feng, V.V. Kuryatkov, D.M. Rosenbladt, N. Stojanovic, S.a. Nikishin, M. Holtz, Diverse facets of InGaN quantum well microrings grown by selective area epitaxy, J. Appl. Phys. 105 (2009) 123524, http://dx.doi.org/10.1063/1.3153982.
[24] G. Naresh-Kumar, D. Thomson, J. Bruckbauer, P.R. Edwards, B. Hourahine, R.W. Martin, Electron channelling contrast imaging for III-nitride thin film structures, Mater. Sci. Semicond. Process. 47 (2016) 44–50, http://dx.doi.org/10.1016/j.mssp.2016.02.007.
[25] G. Naresh-Kumar, J. Bruckbauer, P.R. Edwards, S. Kraeusel, B. Hourahine, R.W. Martin, et al., Coincident electron channeling and cathodoluminescence studies of threading dislocations in GaN, Microsc. Microanal. 20 (2014) 55–60, http://dx.doi.org/10.1017/S1431927613013755.
[26] K. Motoki, T. Okahisa, S. Nakahata, N. Matsumoto, H. Kimura, H. Kasai, et al., Growth and characterization of freestanding GaN substrates, J. Cryst. Growth 237–239 (2002) 912–921, http://dx.doi.org/10.1016/S0022-0248(01)02078-4.
[27] E.B. Yakimov, Investigation of electrical and optical properties in semiconductor structures via SEM techniques with high spatial resolution, J. Surf. Investig. X-Ray, Synchrotron Neutron Tech. 6 (2012) 887–889, http://dx.doi.org/10.1134/S1027451012110158.
[28] H. Fujikura, K. Iizuka, S. Tanaka, Realization of low dislocation GaN/sapphire wafers by 3-step metalorganic vapor phase epitaxial growth with island induced dislocation control, Jpn. J. Appl. Phys. 42 (2003) 2767–2772, http://dx.doi.org/10.1143/JJAP.42.2767.
[29] Q. Li, J.J. Figiel, G.T. Wang, Dislocation density reduction in GaN by dislocation filtering through a self-assembled monolayer of silica microspheres, Appl. Phys. Lett. 94 (2009) 231105, http://dx.doi.org/10.1063/1.3152012.
[30] H. Ji, M. Kuball, R.A. Burke, J.M. Redwing, Vibrational and optical properties of GaN nanowires synthesized by Ni-assisted catalytic growth, Nanotechnology 18 (2007) 445704, http://dx.doi.org/10.1088/0957-4484/18/44/445704.
[31] H. Harima, Properties of GaN and related compounds studied by means of Raman scattering, J. Phys.: Condens. Matter 14 (2002) R967–R993, http://dx.doi.org/10.1088/0953-8984/14/38/201.
[32] T. Kozawa, T. Kachi, H. Kano, H. Nagase, N. Koide, K. Manabe, Thermal stress in GaN epitaxial layers grown on sapphire substrates, J. Appl. Phys. 77 (1995) 4389, http://dx.doi.org/10.1063/1.359465.
[33] T.B. Wei, Y. Chen, Q. Hu, J.K. Yang, Z.Q. Huo, R.F. Duan, et al., Hydride vapor phase epitaxy of strain-reduced GaN film on nano-island template produced using self-assembled CsCl nanospheres, Mater. Lett. 68 (2012) 327–330, http://dx.doi.org/10.1016/j.matlet.2011.10.056.